

# OPTIMIZING THE ATOMIC LAYER DEPOSITION OF ALUMINA ON PEROVSKITE NANOCRYSTAL FILMS BY USING O<sub>2</sub> AS A MOLECULAR PROBE

Seryio Saris<sup>1</sup>, Sanduni T. Dona<sup>1</sup>, Valerie Niemann<sup>1</sup>, Anna Loiudice<sup>1</sup>, Raffaella Buonsanti<sup>1</sup>

## AFFILIATIONS

<sup>1</sup> Laboratory of Nanochemistry for Energy Research, Institute of Chemical Sciences and Engineering, Ecole Polytechnique Fédérale de Lausanne (EPFL), Sion CH-1950, Switzerland

## ABSTRACT

Encapsulation methods have shown to be effective in imparting improved stability to metal-halide perovskite nanocrystals (NCs). Atomic layer deposition (ALD) of metal oxides is one of the promising approaches for such encapsulation, yet better control on the process parameters are required to achieve viable lifetimes for a number of optoelectronic and photocatalytic applications. Herein, we optimize the ALD process of amorphous aluminum oxide (AlO<sub>x</sub>) as an encapsulating layer for CsPbBr<sub>3</sub> NC thin films by using oxygen (O<sub>2</sub>) as a molecular diffusion probe to assess the uniformity of the deposited AlO<sub>x</sub> layer. When O<sub>2</sub> reaches the NC surface, it extracts the photogenerated electrons, thus quenching the PL of the CsPbBr<sub>3</sub> NCs. As the quality of the ALD layer improves, less quenching is expected. We compare three different ALD deposition modes. We find that the low temperature/high temperature and the exposure modes improve the quality of the alumina as a gas barrier when compared with the standard mode. We attribute this result to a better diffusion of the ALD precursor throughout the NC film.

## INTRODUCTION

In recent years, metal halide perovskites have captured interest as ideal candidates for a broad range of optoelectronic and photonic applications.<sup>1-4</sup> These semiconductors exhibit high defect tolerance, such that their optical properties are preserved in the midst of structural irregularities, i.e. point defects<sup>5-7</sup> and grain boundaries.<sup>8,9</sup> High carrier mobilities and large diffusion lengths are also found in perovskite, making them unique materials.<sup>7,8</sup> Of particular note, metal halide perovskite nanocrystals (NCs) can be obtained through colloidal chemistry; their electronic structure and concomitant optical properties are tailored through synthetic control of size, shape, and composition.<sup>10-16</sup> These properties have led to the use of perovskite NCs as photoactive components in technologies such as light-emitting diodes,<sup>17,18</sup> solar cells,<sup>3,19</sup> and photocatalysts.<sup>20-22</sup>

Amidst captivating photophysical properties and facile synthetic and processing requirements, perovskite NCs have an additional key feature, which can be regarded as high reactivity or instability, depending on the ultimate goal.<sup>8,23</sup> Their structure is sensitive to its environment, rapidly destabilizing under conditions that include the presence of air and water, irradiation, and high temperatures. This sensitivity challenges not only their application, but also the achievement of a full understanding of their optoelectronic properties, due to possible structural and compositional changes during illumination.<sup>23</sup> Several strategies have been employed to stabilize CsPbX<sub>3</sub> NCs (X=Br, Cl, I), including ligand design,<sup>24–26</sup> synthetic modification,<sup>27–29</sup> and encapsulation in to a matrix.<sup>23,30–35</sup> We have demonstrated amorphous alumina (AlO<sub>x</sub>) deposited by low-temperature atomic layer deposition (ALD) as one of the promising encapsulation matrix.<sup>34</sup> This approach has major advantages to other stabilization strategies because it is uniform and conformal in nature and because it prevents particle aggregation during the coating process. In addition, it imparts enhanced stability to the perovskite NCs against air, water, light, and high temperatures. The alumina protection layer developed in our first work lasted around few months in air and one hour in water.<sup>34</sup> While remarkable, further improvements of the deposition process are necessary to achieve viable lifetimes for optoelectronic and photocatalytic applications. Developing methods to assess the barrier properties of encapsulating layers on perovskite NCs is crucial to this goal.

Herein, we optimize the above-mentioned ALD protection scheme for CsPbBr<sub>3</sub> NC films by using O<sub>2</sub> as a molecular diffusion probe to assess the uniformity of the encapsulating AlO<sub>x</sub> layer. The O<sub>2</sub> quenches the PL by extracting photogenerated charges.<sup>35,36</sup> The better the gas barrier properties of ALD layer are, the less quenching is expected when the CsPbBr<sub>3</sub>/AlO<sub>x</sub> nanocomposites are exposed to an O<sub>2</sub>-rich atmosphere.<sup>35,36</sup> First, we test three different ALD modes, namely the “standard” mode, the low temperature/high temperature mode and the exposure mode. The standard mode is based on our previous work.<sup>34</sup> Here, a pulse of trimethylaluminum (TMA) is followed by a purging step under vacuum before a pulse of water and a final purging. The deposition is performed at 50°C, which was needed to prevent any structural degradation of the perovskite NCs. In the low temperature/high temperature mode, the first half of the deposition is performed at 50°C and the second half at 100°C. Finally, in the exposure mode the TMA and water pulses are followed by a waiting time before the purging, which is referred to as “diffusion” step and provides time for precursor diffusion into the pores of the CsPbBr<sub>3</sub> NC film. We then use the PL quenching upon exposure to O<sub>2</sub> to probe the quality of the alumina ALD layer as a gas diffusion barrier. We find that both the low temperature/high

temperature and the exposure modes allow around a 5-fold improvement in comparison with the standard mode.

## **I. MATERIALS AND METHODS**

### **A. General**

The following materials were used without further purification unless otherwise stated. Cesium carbonate ( $\text{Cs}_2\text{CO}_3$ , 99.9%, Alfa Aesar), lead bromide ( $\text{PbBr}_2$ , 99.9%, Sigma Aldrich), 1-octadecene (ODE, tech. grade 90%, Acros Organics), oleic acid (OLAC, tech. grade 90%, Sigma Aldrich), oleylamine (OLAM, tech. grade 70%, Sigma Aldrich), trimethylaluminium (TMA, 98%, Strem), 3-mercaptopropyl trimethoxysilane (MPTMS, 95%, Sigma Aldrich), hexane (anhydrous, >96%, TCI), acetone (anhydrous, 99.8%, Fischer Sci.), octane (anhydrous,  $\geq 99\%$ , Sigma Aldrich).

### **B. Synthesis of $\text{CsPbBr}_3$ NCs**

$\text{CsPbBr}_3$  NCs were synthesized with minor modification to what has been previously reported by Protesescu et al.<sup>10</sup>  $\text{Cs}_2\text{CO}_3$  (0.8g), OLAC (2.5 mL) and ODE (80 mL) were stirred under vacuum for 1h at 120 °C. The flask was then purged with  $\text{N}_2$  and the reaction temperature was increased up to 150 °C. This temperature was maintained until the full dissolution of the  $\text{Cs}_2\text{CO}_3$  powder and the formation of a clear Cs-OLAC solution. Consecutively, the temperature was decreased and kept at 120 °C until further use. In a separate reaction flask,  $\text{PbBr}_2$  (0.35g) and ODE (25 mL) were mixed and degassed for 1h at 120 °C. The flask was then purged with  $\text{N}_2$  at constant flow. This step was followed by the addition of equal volumes of OLAC and OLAM (1.5 mL each). The temperature was subsequently raised to 160 °C after the complete dissolution of  $\text{PbBr}_2$  powder. The previously prepared Cs-OLAC solution (2 mL) was then swiftly injected into the reaction mixture and quenched by an ice bath after 5s of injection. The crude solution was then precipitated by centrifugation at 6000 rpm for 20 mins, re-dispersed in hexane, washed with acetone, and finally centrifuged at 6000 rpm to be re-dispersed in hexane. The NC were characterized by transmission electron microscopy (TEM) where images were recorded on an Analytical JEOL-2100F FETEM using a beam energy of 200 kV, equipped with a Gatan camera. Samples were drop-casted on a copper TEM grid (Ted Pella, Inc.) prior to imaging. Size statistics was performed using the software ImageJ and counting at least 100 particles per sample. Inductively coupled plasma atomic emission spectroscopy (ICP-AES) experiments

were performed on an Agilent Model5100 instrument to obtain NC concentrations. Further dilutions were performed in accordance with the film preparation process.

### **C. CsPbBr<sub>3</sub> NC Film Preparation and Characterization**

Glass and p-doped silicon (Si) substrates were sonicated and rinsed with successive cycles of acetone and isopropanol to ensure a clean surface. In cases where surface treatment was necessary, it was performed by keeping the cleaned substrates overnight in a 0.02M MPTPMS solution in toluene.<sup>37</sup> The substrates were washed with toluene the following day and dried before spin-coating was performed. Colloidal perovskite NCs were then spin-coated, with an optimized Pb concentration of 0.5 mgmL<sup>-1</sup> and a solvent volume ratio of 1:3 hexane/octane unless otherwise noted, on 1 x 1 cm<sup>2</sup> substrates at 1000 rpm for 45 seconds and subsequently at 2500 rpm to assist full evaporation. Additionally, the dip-coating process has been detailed in the supplementary material (see Table S1). The NC films were then characterized by scanning electron microscopy (SEM), atomic force microscopy (AFM) and UV-visible absorption spectroscopy. Following this order, SEM images were acquired on a FEI Teneo, which uses an inlens detector at a beam energy of 2 keV and a beam current of 13 pA. AFM measurements were performed on a Nanoscope IIIa (Veeco, USA), operated in tapping-mode, with Nanosensors PP-NCSTR AFM probes. Thin lines were scratched on the samples in order to reveal the silicon substrate. The mapping was carried-out at the edge of the lines. The maps were finally flattened prior to the measurements of the film thickness. UV-Visible absorption measurements were performed in solution using a quartz cuvette and in film on glass substrates in transmission mode using a Perkin Elmer Lambda 950 Spectrophotometer equipped with deuterium and tungsten halide as light sources, and a photomultiplier (PMT) with pertier-controlled PbS detector.

### **D. Atomic Layer Deposition (ALD)**

All atomic layer deposition (ALD) processes were performed on a Savannah-200 ALD system from Cambridge Nanotech Inc. Three main deposition modes were employed, as also summarized in Scheme I. These three modes were named as standard, low temperature/high temperature and exposure mode. Firstly, the depositions in standard mode were performed following our previously published work.<sup>34</sup> Amorphous AlO<sub>x</sub> was deposited on top of the CsPbBr<sub>3</sub> NC films. Trimethylaluminum (TMA) and ultrapure water were used as aluminium

and oxygen sources, respectively. The reaction chamber was kept at a temperature of 50 °C and an N<sub>2</sub> flow of 20 sccm. Each deposition cycle consisted of a TMA pulse time (t<sub>1</sub>), a first purging time (pt<sub>1</sub>), a water pulse time (t<sub>2</sub>) and a second purging time (pt<sub>2</sub>), where t<sub>1</sub>= 0.01s, pt<sub>1</sub>= 10s, t<sub>2</sub>= 0.015s and pt<sub>2</sub>= 60s. The thickness of the amorphous AlO<sub>x</sub> layer was controlled by varying the number of ALD cycles, up to 100 cycles. Secondly, the depositions in low temperature/high temperature mode were performed in two steps. First half of the deposition (e.g 50 cycles) was identical to the standard mode, while the second half of the deposition (e.g the remaining 50 cycles in 100 cycle deposition) was performed at a higher temperature of 100 °C instead of 50 °C. The standard recipe for Al<sub>2</sub>O<sub>3</sub> in the Savannah-200 ALD system is set at 80°C, so temperatures higher than 100°C were not considered for this study. Thirdly, the depositions in exposure mode were performed with an additional diffusion time (dt) for the precursors, in which the evacuation pump was switched off for a specified amount of time. The optimized exposure mode parameters are as follows, unless otherwise stated; TMA pulse time (t<sub>1</sub>)=0.01s, TMA diffusion time (dt<sub>1</sub>) = 5s, TMA purge time (pt<sub>1</sub>) = 10s, water pulse time (t<sub>2</sub>)=0.010s, water diffusion time (dt<sub>2</sub>)= 5s, water purging time (pt<sub>2</sub>)=60s. Exposure mode deposition was done at a temperature of 50 °C and an N<sub>2</sub> flow of 15 sccm.

#### **E. Photoluminescence Experiments under O<sub>2</sub>/vacuum**

PL measurements were performed under a controlled atmosphere by using an air-tight cell connected both to a vacuum pump and an O<sub>2</sub> tank through a valve. The atmosphere was cycled between O<sub>2</sub>/vacuum (10<sup>-3</sup> bar) by switching the valve. Steady-state PL measurements were carried out using a Perkin Elmer LS55 fluorometer equipped with a Xe arc lamp and a PMT detector, at an excitation wavelength of 420-nm. It must be noted that for stability experiments the initial PL intensities were taken to be the maximum counts for a given emission slit size. All measurements were carried out at a room temperature of approximately 20 °C.

## II. RESULTS AND DISCUSSION

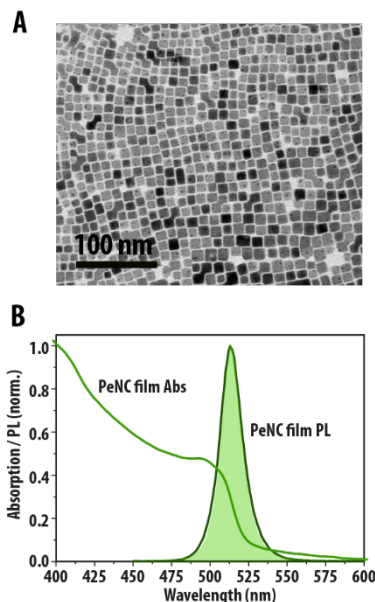


**FIG.1** (A) Transmission electron microscopy (TEM) image of pristine  $\text{CsPbBr}_3$  perovskite nanocrystals (PeNCs) and (B) their corresponding absorption and photoluminescence spectra.

TEM images of the as-synthesized  $\text{CsPbBr}_3$  NCs, from here on referred to as PeNCs, can be seen in Figure 1A. PeNCs possess a cubic morphology with an average edge length of 9.1 nm and low poly-dispersity, with a standard deviation of  $\pm 1.4$  nm. The PeNCs were spin-coated on glass and Si substrates, as detailed in the materials and methods section. The corresponding PeNC film absorption and emission spectra are shown in Figure 1B. For an optimally conformal and pinhole-free ALD  $\text{AlOx}$ , it is crucial to have uniform NC films in order to facilitate the homogenous growth of the stepwise deposition. Strict control over the thickness of the NC film is also advantageous in order to avoid undesired effects of different  $\text{AlOx}$  growth rates at different thickness that would result in an inhomogeneous ALD infilling and uneven coating. Due to the ionic nature of perovskites and the labile binding of the ligands,<sup>38</sup> it is not straightforward to achieve such uniform films with conventional layer-by-layer and electrostatic assembly techniques.<sup>39,40</sup> For that purpose, a number of parameters were screened during the initial phases of the spin-coating process, and the resulting PeNC films were checked by scanning electron microscopy (SEM) for optimal uniformity and thickness. These parameters include the concentration of the PeNC solution (Figure S1), the hexane-to-octane

volume ratio of the same (Figure S2) and surface treatments of the substrates (Figure 2A and 2B). Modifying the concentration and the hexane-to-octane volume ratio helped in achieving a more even distribution of PeNCs on the substrates, yet large pinholes (500nm-2 $\mu$ m) and uncovered areas could not be avoided, as evident in the SEM images (Figures S1 and S2). Increasing the PeNC concentration and the hexane amount in the spin-coating solution resulted in the inhomogeneous stacking of the NCs, instead of a uniform spreading on the substrate surface. This effect was attributed mostly to the low affinity of the PeNCs to the substrate surface.

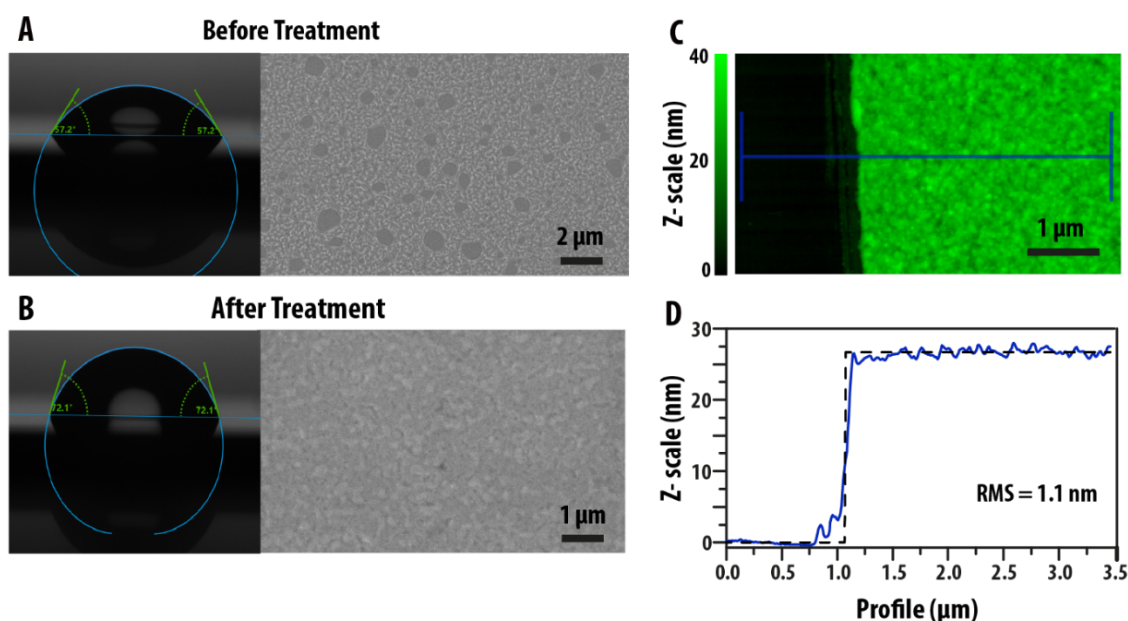


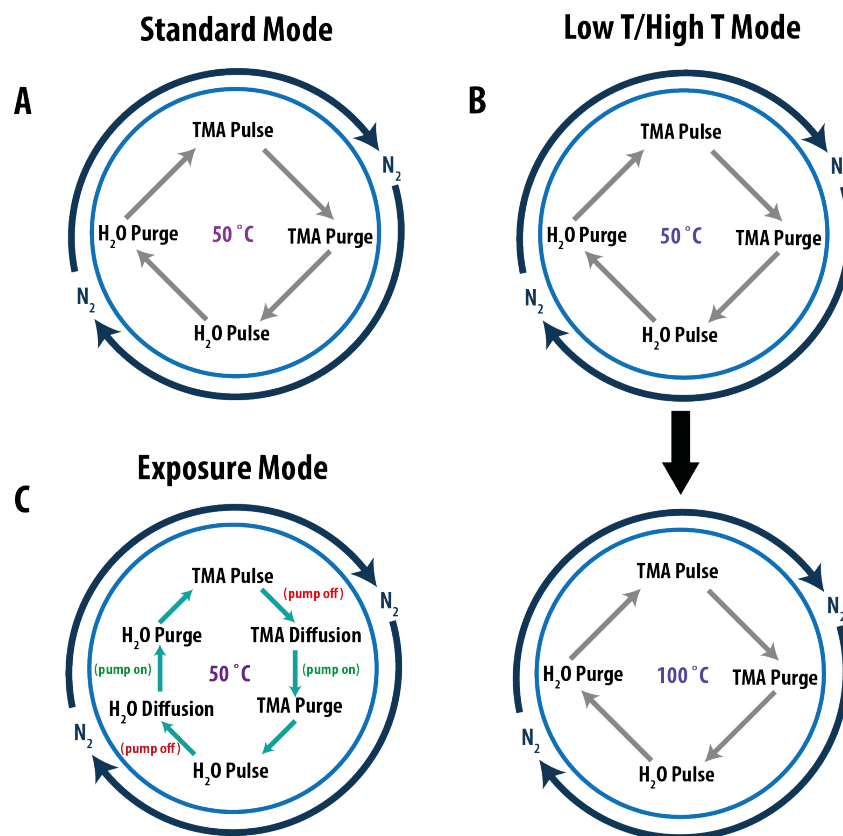
**FIG.2** (A,B) Water contact-angle measurements and SEM images of spin-coated PeNC films on silicon substrate without and with the 3-mercaptopropyl trimethoxysilane treatment, respectively. (C) AFM image of the PeNC film in (B) and (D) the corresponding profile showing the thickness of the film.

In order to improve the adhesion of the PeNCs to the substrate surface, the substrates were treated with 3-mercaptopropyl trimethoxysilane (MPTMS) prior to spin-coating (see Materials & Methods section for details). To ensure that the surface treatment had altered the surface properties of the substrate, water contact angle measurements were performed to quantify wettability. A static contact angle is defined by fitting Young-Laplace equation around the water droplet. As shown in Figure 2A and 2B, the water contact angle on silicon substrate increased from 57° to 72° after the silane treatment, indicating lower surface wetting and hence higher hydrophobicity, which successfully demonstrates the attachment of the silane molecules on the substrate surface. It is clearly visible from the SEM images in Figure 2A and 2B that

surface treatment improves the film uniformity and eliminates most of the pinholes and uncovered areas. Additional characterization of the PeNC film in Figure 2B by AFM profiling shows a relatively smooth surface and a thickness of  $\sim 27$  nm and root-square-roughness of 1.1 nm, suggesting the formation of a compact three monolayer-thick NC film. PeNC single monolayer films were successfully obtained by switching from spin-coating to dip-coating. SEM and AFM analysis of the resulting dip-coated PeNC films, after optimization, are reported in Figures S3-4 and Table S1. For the ALD deposition and following PL experiments, spin-coated films were preferred over the dip-coated monolayers for the lowest material waste and higher reproducibility.

The next step involves the deposition of amorphous AlOx on the PeNC films. The three different ALD deposition modes used in this study are depicted in Scheme 1. In the standard mode, shown in Scheme 1A, the deposition occurs at a continuous flow of the carrier N<sub>2</sub> gas at 50 °C. The reaction chamber is constantly being evacuated by a vacuum pump, hence the diffusion time of the reaction precursors (TMA and H<sub>2</sub>O) is limited. One way to design ALD processes that induce more homogenous and uniform growth of AlOx on top of high-aspect ratio structures, as the NC films are, is to play with the process temperature. Higher temperature will facilitate the ALD precursor diffusion, thus improving the overall coverage. For the PeNCs, increasing the temperature is an extended challenge as it would result in sintering of the NCs. Accordingly, two different modes are proposed aiming at improving the homogeneity of the deposition, as shown in Scheme 1B-C, denoted as low temperature/high temperature and exposure modes, respectively. A number of reports, including ours, have shown that the NC films become more resistant to sintering upon infilling with ALD oxides.<sup>34,41–43</sup> Hence, the low temperature/high temperature mode (Scheme 1B) is presumed to take advantage of the initial infilling step at 50 °C, that thermally stabilizes the PeNC, after which the deposition temperature can be increased to 100 °C for a more homogenous coating of AlOx due to the enhanced diffusion of the precursors at this temperature. Alternatively, in the exposure mode (Scheme 1C) additional diffusion time for the precursors is introduced to the standard mode, by momentarily switching off the vacuum pump. The exposure mode has been well-established for the coating high-aspect ratio structures.<sup>44–46</sup>





**SCHEME 1.** Schematic illustration of the three ALD modes tested in this study. (A) Standard continuous mode where the TMA/H<sub>2</sub>O pulses are followed by purge times, at a deposition temperature of 50 °C. In continuous mode the evacuation pump is always on, to allow constant flow of the reaction precursors throughout the deposition. (B) Low temperature/high temperature mode which is a two-step standard deposition process where the first half of the deposition occurs at 50 °C, while the second half occurs at 100 °C. (C) Exposure mode where an additional diffusion time is introduced compared to the standard mode by switching off the evacuation pump after TMA/H<sub>2</sub>O pulses.

O<sub>2</sub> was then used as a molecular probe in order to compare and contrast the ability of the proposed ALD modes to grow gas diffusion barriers. Recent reports have demonstrated reduction in the PL of CsPbBr<sub>3</sub> NCs in the presence of molecular O<sub>2</sub>.<sup>35,36</sup> The authors have suggested that this behavior is due to the interaction of O<sub>2</sub> with the NC surface. Specifically, O<sub>2</sub> extracts the photogenerated electrons of the PeNC thus slowing down the radiative recombination rate. Hence, we hypothesize that one can probe the diffusion barrier properties of AlOx in the PeNC/AlOx nanocomposites synthesized with different deposition modes by exploiting the interaction of O<sub>2</sub> with PeNC surface. The better the barrier is, the lower the PL quenching is expected. Figure 3 reports such an experiment performed for the nanocomposites synthesized by the standard deposition mode (Scheme 1A) with different ALD cycles. The greater the number of cycles is, the thicker the ALD coating is according to previously derived

growth rate.<sup>34</sup> A maximum of 100 ALD cycles (~10 nm AlOx coating layer) was used to avoid having a very thick coating layer that would be limiting for most applications. The changes in PL were monitored in a custom-made chamber which can be switched between vacuum/O<sub>2</sub> environments. In agreement with the previous studies on bare PeNC films<sup>36,37</sup>, PL quenching occurs when the samples are exposed to O<sub>2</sub>. This quenching is mostly reversible and the PL quickly returns to its original value when O<sub>2</sub> is again replaced by vacuum. The data relative to the uncoated PeNC films are reported in Figure S5. In the PeNC/AlOx nanocomposites a thickness dependence of this phenomenon is observed. As the number of ALD cycles increases, the overall PL reduction under O<sub>2</sub> occurs to a lesser extent. This behavior indicates that the thicker the AlOx coating is and the more efficient barrier towards the diffusion of O<sub>2</sub> is. Nevertheless, the AlOx deposited by the standard mode never completely blocks oxygen to access the PeNC surface.

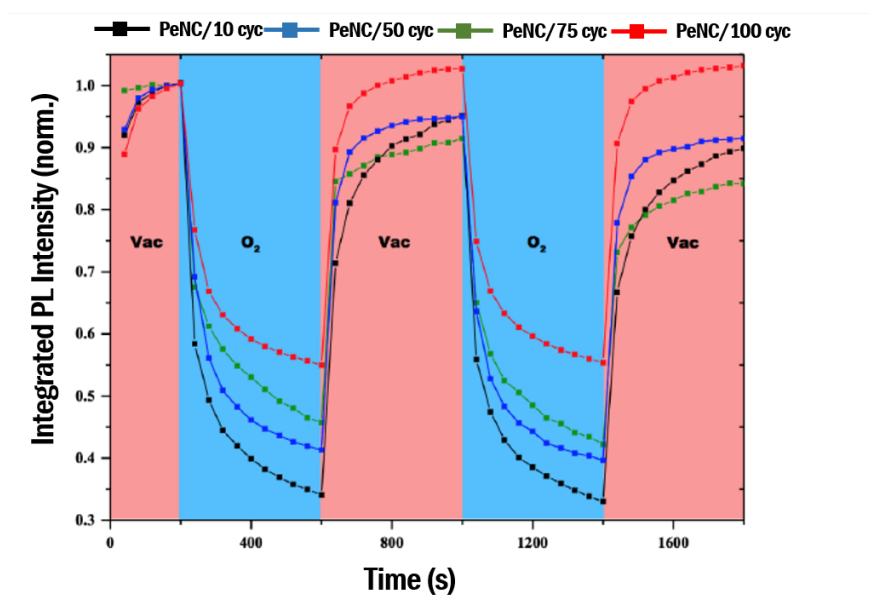


**FIG.3** PL changes of PeNC/AlOx nanocomposites prepared with different number of ALD cycles during vacuum/O<sub>2</sub> cycling.

Next, the gas barrier properties of the AlOx layers prepared by the low temperature/high temperature and the exposure ALD modes were tested. The PL measurement results are shown in Figure 4. Compared to the PeNC/100cyc (standard mode) samples, both PeNC/100 cyc (high T) and PeNC/100cyc (expo) show an almost negligible PL reduction under O<sub>2</sub>. It is noted that a number of parameters were tested (e.g diffusion times, carrier N<sub>2</sub> flow, water purge times) to optimize the deposition conditions for the exposure mode and further details are reported in Figures S6-8. The considerable improvement in the barrier properties with the low

temperature/high temperature and the exposure modes is mainly ascribed to the more effective diffusion of the ALD precursors, i.e. TMA and water, into the pores of PeNC film which results in a more conformal deposition of the AlOx. One final point should be made with regards to the photoluminescence quantum yield (PLQY) of each deposition mode in air (see Table S2). It is evident that there is a 40% decrease in the PLQY of the PeNC/AlOx nanocomposites compared to pristine films, regardless of the deposition mode. This effect has been previously reported and attributed to a combination of ligand desorption in the vacuum step and TMA interaction with the NC surface, where both cases introduce surface trap states into the electronic structure.<sup>29,34,47,48</sup>

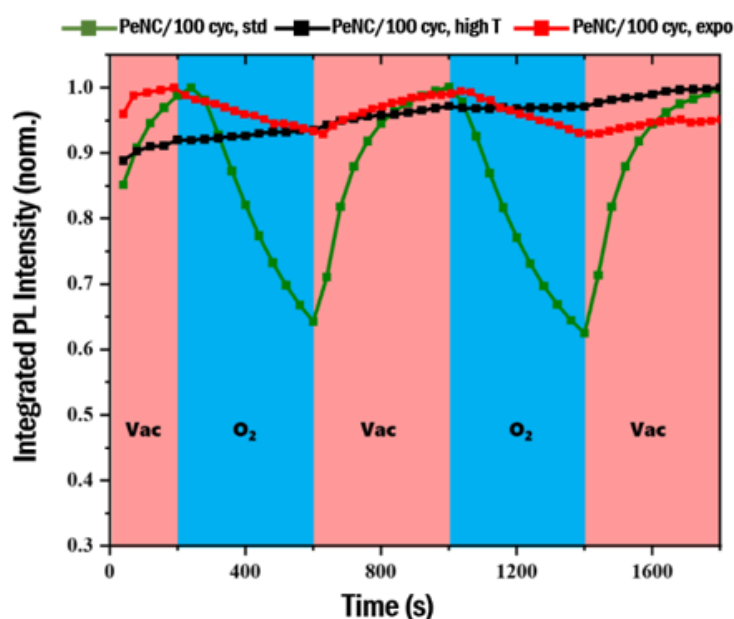


**FIG.4** (A) PL changes of PeNC/AlOx nanocomposites with 100 cycles of AlOx deposited via the standard mode (std), the low T/high T mode (high T) and the exposure mode (expo).

### III. CONCLUSION

In conclusion, the gas barrier properties of AlO<sub>x</sub> deposited via three different ALD modes (i.e. standard, high temperature/low temperature, exposure) to form PeNC/AlOx nanocomposite were tested using O<sub>2</sub> as a molecular probe. First, uniform PeNC films were fabricated using spin-coating on silane-functionalized silicon substrates. This step was crucial for ensuring homogenous infilling of the PeNC films as well as the uniform growth of AlOx during the ALD process which allows to reliably compare the three modes. Then, the PL changes of these nanocomposite films were carefully monitored during vacuum/O<sub>2</sub> cycling. We demonstrate that the AlOx layer reduces such PL quenching by acting as a gas diffusion barrier.

The thicker the AlO<sub>x</sub> layer is, the less the PL is reduced upon O<sub>2</sub> exposure. Comparing the three deposition modes, the low temperature/high temperature and the exposure modes rendered the PeNC films almost insensitive to the changes in the surrounding atmosphere. This drastic improvement was attributed to the better diffusion of the ALD precursors into the pores/interstices of the PeNC film, resulting in better surface passivation as well as more conformal growth of AlO<sub>x</sub>. In addition to reporting an improvement in the barrier properties of alumina coating via ALD, this study presents a novel way to use O<sub>2</sub> as a molecular probe to assess the barrier properties of encapsulating layers for improving the stability of quantum dot films.

## **SUPPLEMENTARY MATERIAL**

See supplementary material for additional scanning electron microscopy and atomic force microscopy images and supporting photoluminescence experiments, as referred to in the main text.

## **ACKNOWLEDGEMENTS**

This work is financially supported by the Swiss National Science Foundation (AP Energy Grant, project number PYAPP2\_166897/1). Valerie Niemann acknowledges support from the Fullbright U.S. Student program and Swiss Federal Commission for Scholarships for Foreign Students. Dr. Mounir Mensi is acknowledged for the acquisition of the AFM data.

## **REFERENCES**

- <sup>1</sup> S.D. Stranks and H.J. Snaith, *Nat. Nanotechnol.* **10**, 391 (2015).
- <sup>2</sup> W. Zhang, G.E. Eperon, and H.J. Snaith, *Nat. Energy* **1**, 16048 (2016).
- <sup>3</sup> Q. Zhao, A. Hazarika, X. Chen, S.P. Harvey, B.W. Larson, G.R. Teeter, J. Liu, T. Song, C. Xiao, L. Shaw, M. Zhang, G. Li, M.C. Beard, and J.M. Luther, *Nat. Commun.* **10**, (2019).
- <sup>4</sup> X. He, Y. Qiu, and S. Yang, *Adv. Mater.* **29**, (2017).
- <sup>5</sup> J. Kang and L.W. Wang, *J. Phys. Chem. Lett.* **8**, 489 (2017).
- <sup>6</sup> A. Walsh, D.O. Scanlon, S. Chen, X.G. Gong, and S.H. Wei, *Angew. Chemie - Int. Ed.* **54**,

1791 (2015).

<sup>7</sup> G.R. Yettapu, D. Talukdar, S. Sarkar, A. Swarnkar, A. Nag, P. Ghosh, and P. Mandal, *Nano Lett.* **16**, 4838 (2016).

<sup>8</sup> H. Huang, M.I. Bodnarchuk, S. V. Kershaw, M. V. Kovalenko, and A.L. Rogach, *ACS Energy Lett.* **2**, 2071 (2017).

<sup>9</sup> Y. Guo, Q. Wang, and W.A. Saidi, *J. Phys. Chem. C* **121**, 1715 (2017).

<sup>10</sup> L. Protesescu, S. Yakunin, M.I. Bodnarchuk, F. Krieg, R. Caputo, C.H. Hendon, R.X. Yang, A. Walsh, and M. V. Kovalenko, *Nano Lett.* **15**, 3692 (2015).

<sup>11</sup> O. Vybornyi, S. Yakunin, and M. V. Kovalenko, *Nanoscale* **8**, 6278 (2016).

<sup>12</sup> J. Shamsi, A.S. Urban, M. Imran, L. De Trizio, and L. Manna, *Chem. Rev.* **119**, 3296 (2019).

<sup>13</sup> G. Nedelcu, L. Protesescu, S. Yakunin, M.I. Bodnarchuk, M.J. Grotevent, and M. V. Kovalenko, *Nano Lett.* **15**, 5635 (2015).

<sup>14</sup> S. Das Adhikari, A.K. Guria, and N. Pradhan, *J. Phys. Chem. Lett.* **10**, 2250 (2019).

<sup>15</sup> S. Ghosh and L. Manna, *Chem. Rev.* **118**, 7804 (2018).

<sup>16</sup> W. Van der Stam, J.J. Geuchies, T. Altantzis, K.H.W. Van Den Bos, J.D. Meeldijk, S. Van Aert, S. Bals, D. Vanmaekelbergh, and C. De Mello Donega, *J. Am. Chem. Soc.* **139**, 4087 (2017).

<sup>17</sup> S.T. Ochsenbein, F. Krieg, Y. Shynkarenko, G. Rainò, and M. V. Kovalenko, *ACS Appl. Mater. Interfaces* **11**, 21655 (2019).

<sup>18</sup> X. Zhang, B. Xu, J. Zhang, Y. Gao, Y. Zheng, K. Wang, and X.W. Sun, *Adv. Funct. Mater.* **26**, 4595 (2016).

<sup>19</sup> X. Ling, S. Zhou, J. Yuan, J. Shi, Y. Qian, B.W. Larson, Q. Zhao, C. Qin, F. Li, G. Shi, C. Stewart, J. Hu, X. Zhang, J.M. Luther, S. Duhm, and W. Ma, *Adv. Energy Mater.* **1900721**, 1 (2019).

<sup>20</sup> X. Zhu, Y. Lin, J. San Martin, Y. Sun, D. Zhu, and Y. Yan, *Nat. Commun.* **10**, 1 (2019).

<sup>21</sup> Y.F. Xu, M.Z. Yang, B.X. Chen, X.D. Wang, H.Y. Chen, D. Bin Kuang, and C.Y. Su, *J. Am. Chem. Soc.* **139**, 5660 (2017).

- <sup>22</sup> K. Chen, X. Deng, G. Dodekatos, and H. Tüysüz, *J. Am. Chem. Soc.* **139**, 12267 (2017).
- <sup>23</sup> W. Lv, L. Li, M. Xu, J. Hong, X. Tang, L. Xu, Y. Wu, R. Zhu, R. Chen, and W. Huang, *Adv. Mater.* **1900682**, 1 (2019).
- <sup>24</sup> J. Pan, L.N. Quan, Y. Zhao, W. Peng, B. Murali, S.P. Sarmah, M. Yuan, L. Sinatra, N.M. Alyami, J. Liu, E. Yassitepe, Z. Yang, O. Voznyy, R. Comin, M.N. Hedhili, O.F. Mohammed, Z.H. Lu, D.H. Kim, E.H. Sargent, and O.M. Bakr, *Adv. Mater.* **28**, 8718 (2016).
- <sup>25</sup> J. Pan, Y. Shang, J. Yin, M. De Bastiani, W. Peng, I. Dursun, L. Sinatra, A.M. El-Zohry, M.N. Hedhili, A.H. Emwas, O.F. Mohammed, Z. Ning, and O.M. Bakr, *J. Am. Chem. Soc.* **140**, 562 (2018).
- <sup>26</sup> H. Sun, Z. Li, L. Kong, B. Wang, C. Zhang, Q. Yuan, S. Huang, Y. Liu, and L. Li, *Chem. Commun.* **54**, 9345 (2018).
- <sup>27</sup> W. Chen, J. Hao, W. Hu, Z. Zang, X. Tang, L. Fang, T. Niu, and M. Zhou, *Small* **13**, 1 (2017).
- <sup>28</sup> M. Meyns, M. Perálvarez, A. Heuer-Jungemann, W. Hertog, M. Ibáñez, R. Nafria, A. Genç, J. Arbiol, M. V. Kovalenko, J. Carreras, A. Cabot, and A.G. Kanaras, *ACS Appl. Mater. Interfaces* **8**, 19579 (2016).
- <sup>29</sup> A. Loiudice, M. Strach, S. Saris, D. Chernyshov, and R. Buonsanti, *J. Am. Chem. Soc.* **141**, 8254 (2019).
- <sup>30</sup> Y. Wei, X. Deng, Z. Xie, X. Cai, S. Liang, P. Ma, Z. Hou, Z. Cheng, and J. Lin, *Adv. Funct. Mater.* **27**, 1 (2017).
- <sup>31</sup> Z. Li, L. Kong, S. Huang, and L. Li, *Angew. Chemie - Int. Ed.* **56**, 8134 (2017).
- <sup>32</sup> H.-C. Wang, S.-Y. Lin, A.-C. Tang, B.P. Singh, H.-C. Tong, C.-Y. Chen, Y.-C. Lee, T.-L. Tsai, and R.-S. Liu, *Angew. Chemie Int. Ed.* **55**, 7924 (2016).
- <sup>33</sup> W. Yang, F. Gao, Y. Qiu, W. Liu, H. Xu, L. Yang, and Y. Liu, *Adv. Opt. Mater.* **1900546**, 1 (2019).
- <sup>34</sup> A. Loiudice, S. Saris, E. Oveisi, D.T.L. Alexander, and R. Buonsanti, *Angew. Chemie - Int. Ed.* **56**, 10696 (2017).
- <sup>35</sup> C. Rodà, A.L. Abdelhady, J. Shamsi, M. Lorenzon, V. Pinchetti, M. Gandini, F. Meinardi, L. Manna, and S. Brovelli, *Nanoscale* **11**, 7613 (2019).

- <sup>36</sup> M. Lorenzon, L. Sortino, Q. Akkerman, S. Accornero, J. Pedrini, M. Prato, V. Pinchetti, F. Meinardi, L. Manna, and S. Brovelli, *Nano Lett.* **17**, 3844 (2017).
- <sup>37</sup> M.C. Weidman, K.G. Yager, and W.A. Tisdale, *Chem. Mater.* **27**, 474 (2015).
- <sup>38</sup> J. De Roo, M. Ibáñez, P. Geiregat, G. Nedelcu, W. Walravens, J. Maes, J.C. Martins, I. Van Driessche, M. V. Kovalenko, and Z. Hens, *ACS Nano* **10**, 2071 (2016).
- <sup>39</sup> M. Gao, J. Sun, E. Dulkeith, N. Gaponik, U. Lemmer, and J. Feldmann, *Langmuir* **18**, 4098 (2002).
- <sup>40</sup> M.A. Kostiainen, P. Hiekkataipale, A. Laiho, V. Lemieux, J. Seitsonen, J. Ruokolainen, and P. Ceci, *Nat. Nanotechnol.* **8**, 52 (2013).
- <sup>41</sup> R. Ihly, J. Tolentino, Y. Liu, M. Gibbs, and M. Law, *ACS Nano* **5**, 8175 (2011).
- <sup>42</sup> Y. Liu, J. Tolentino, M. Gibbs, R. Ihly, C.L. Perkins, Y. Liu, N. Crawford, J.C. Hemminger, and M. Law, *Nano Lett.* **13**, 130307111258007 (2013).
- <sup>43</sup> J.Y. Woo, J. Lee, and C.-S. Han, *Nanotechnology* **24**, 505714 (2013).
- <sup>44</sup> R. Zazpe, M. Knaut, H. Sopha, L. Hromadko, M. Albert, J. Prikryl, V. Gärtnerová, J.W. Bartha, and J.M. Macak, *Langmuir* **32**, 10551 (2016).
- <sup>45</sup> J.R. Bakke, K.L. Pickrahn, T.P. Brennan, and S.F. Bent, *Nanoscale* **3**, 3482 (2011).
- <sup>46</sup> A.F. Palmstrom, P.K. Santra, and S.F. Bent, *Nanoscale* **7**, 12266 (2015).
- <sup>47</sup> B. Yin, B. Sadtler, M.Y. Berezin, and E. Thimsen, *Chem. Commun.* **52**, 11127 (2016).
- <sup>48</sup> Y. Liu, M. Gibbs, C.L. Perkins, J. Tolentino, M.H. Zarghami, J. Bustamante, and M. Law, *Nano Lett.* **11**, 5349 (2011).